Modeling of a hydraulic arresting gear using fluid–structure interaction and isogeometric analysis

Chenglong Wang[a], Michael C.H. Wu[a], Fei Xu[a], Ming-Chen Hsu[a], Yuri Bazilevs[b,*]

[a]*Department of Mechanical Engineering, Iowa State University, 2025 Black Engineering, Ames, IA 50011, USA*
[b]*Department of Structural Engineering, University of California, San Diego, 9500 Gilman Drive, La Jolla, CA 92093, USA*

Abstract

Fluid–structure interaction (FSI) analysis of a full-scale hydraulic arresting gear used to retard the forward motion of an aircraft landing on an aircraft-carrier deck is performed. The simulations make use of the recently developed core and special-purpose FSI techniques for other problem classes, specialized to the present application. A recently proposed interactive geometry modeling and parametric design platform for isogeometric analysis (IGA) is directly employed to create the arresting gear model, and illustrates a natural application of IGA to this problem class. The fluid mechanics and FSI simulation results are reported in terms of the arresting-gear rotor loads and blade structural deformation and vibration. Excellent agreement is achieved with the experimental results for the arresting gear design simulated in this work.

Keywords: Fluid–structure interaction; Hydraulic arresting gear; Isogeometric analysis; Parametric design; NURBS; Hydrodynamic loading

1. Introduction

Military aircraft, during landing on the deck of an aircraft carrier, eject a "hook" that engages a wire connected to a tape drum. The resultant tape-drum angular momentum is transferred to the rotor inside a hydraulic energy absorber (or a hydraulic arresting gear). The rotor, which is a steel structure several feet in diameter, accelerates rapidly, reaching speeds of 800 rpm. The rotor acceleration is then arrested by the drag forces coming from the surrounding water inside the arresting gear. This, in turn, puts the wire in tension and rapidly slows the aircraft forward motion. The rotor speed and blade topology, geometry, and structural design play a critical role in the performance of the device, both in its function to arrest the motion of landing aircraft, as well as in its ability to withstand the internal hydrodynamic loads and perform multiple consecutive aircraft

*Corresponding author
Email address: yuri@ucsd.edu (Yuri Bazilevs)

The final publication is available at Computers & Fluids via http://dx.doi.org/10.1016/j.compfluid.2015.12.004

arrests without failure. As a result, accurate prediction of rotor loads and the structure response to these loads is important, requiring advanced modeling and simulation, which we undertake in this work.

Experimental study of the hydraulic arresting gear presents many challenges, which mainly arise due to the large spatial scales and high rotor speeds involved in the device operation. The fact that the device is completely enclosed complicates the situation further. However, the hydraulic arresting gear lends itself nicely to analysis using computational fluid–structure interaction (FSI). Computational FSI has matured significantly over the last decade and many core and special purpose techniques were developed in this arena, which can be used to address the various challenges involved in the arresting-gear problem (see, e.g., [1–37] and references therein for a sampling of FSI methods developed in recent years.)

In addition to FSI, the present application lends itself nicely to Isogeometric Analysis (IGA) [38, 39], which is a relative newcomer to the field of computational mechanics. The use of IGA enables relatively simple construction of the arresting gear geometric and structural design, its complete surface and volume parameterization, and analysis using the same underlying geometric representation in terms of Non-Uniform Rational B-Splines (NURBS) [40] or T-splines [41, 42].

The paper is outlined as follows. In Section 2, we describe the geometry of the Virginia Tech (VT) arresting gear design [43], which belongs to the Model 64 [44] energy absorber system. We describe a novel technique for IGA analysis-suitable geometry construction of the arresting gear design. We make use of a recently proposed interactive geometry modeling and parametric design platform [45], which is based on the Rhino 3D CAD software [46] with an embedded visual programming tool Grasshopper [47]. Rhino 3D gives the user access to complex geometry modeling functionality with objects such as NURBS and T-splines, while Grasshopper is employed for the generative algorithm approach to arresting-gear geometric design. In Section 3, we present the governing equations involved in the FSI model and summarize the numerical formulations employed. In Section 4, we present the results of standalone fluid and structural mechanics, and FSI analyses of the VT arresting gear at full scale.

2. Geometry Modeling and Meshing for the Arresting Gear FSI Analysis

In this work we simulate the VT arresting gear design described in [43] and shown in Figure 1. We consider a full-scale model with slightly simplified geometry, but with all the important structural components represented. The VT model has experimental data available for hydrodynamic loads acting on the rotor operating at speeds ranging from 200 rpm to 800 rpm, which are typical rotor speeds during the aircraft arrest. The availability of experimental data enables one to perform methods validation at full scale, and to assess the computational effort needed for this challenging problem class.

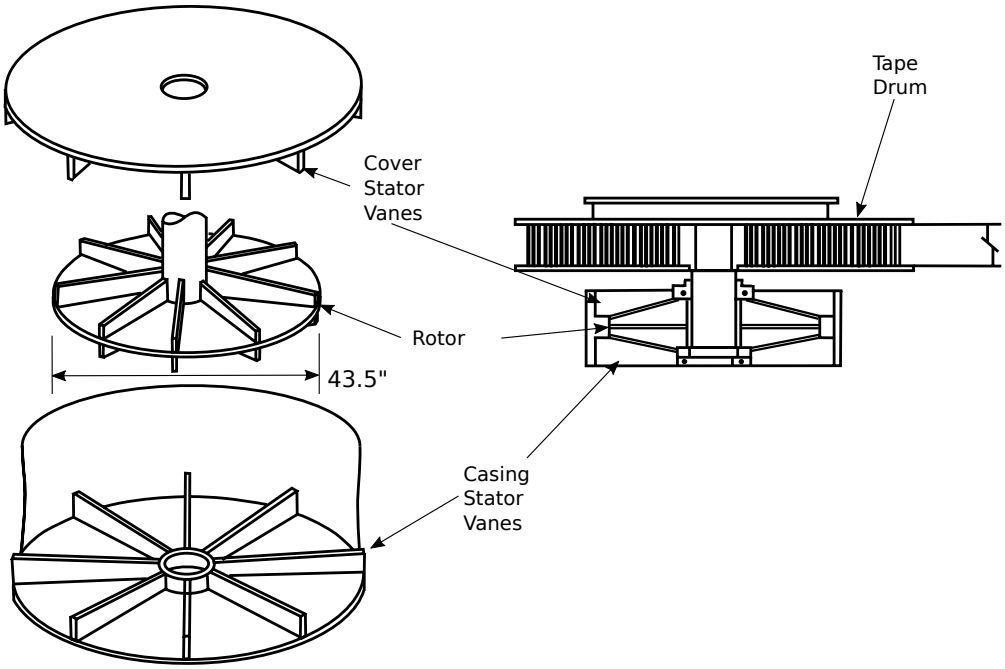

Figure 1: Schematic representation of the VT hydraulic arresting gear [43].

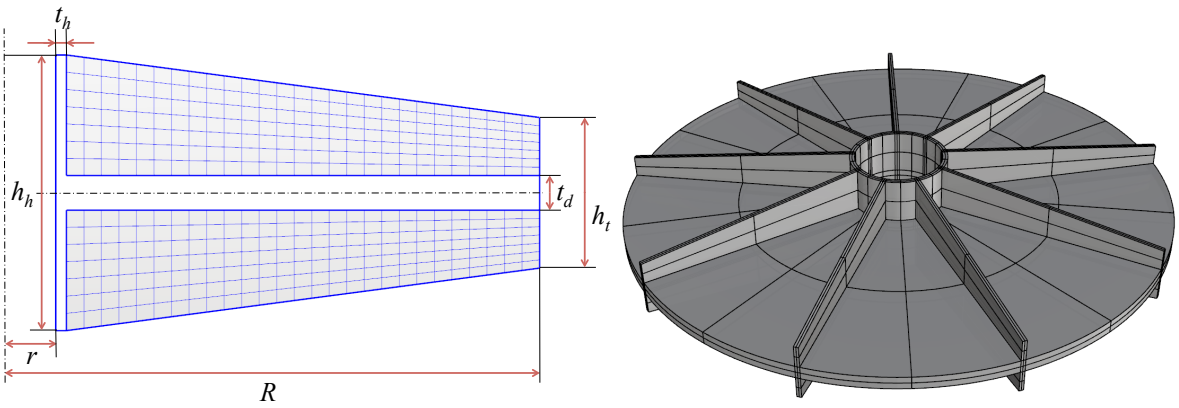

Figure 2: Left: Rotor cross-section with dimensions. Right: Rotor solid model.

Table 1: Arresting gear rotor dimensions.

Parameter	Symbol	Unit (in)
Hub thickness	t_h	0.4
Hub height	h_h	7.96
Inner radius	r	3.48
Outer radius	R	21.75
Disc thickness	t_d	1.0
Tip height	h_t	4.35
Blade thickness	t_b	0.348

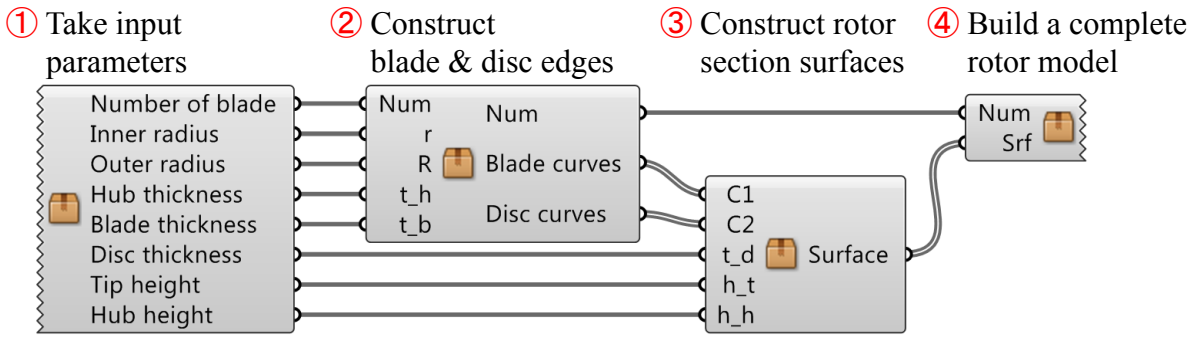

Figure 3: Generative algorithm for parametric geometry design of the arresting gear rotor expressed in a visual programming interface Grasshopper.

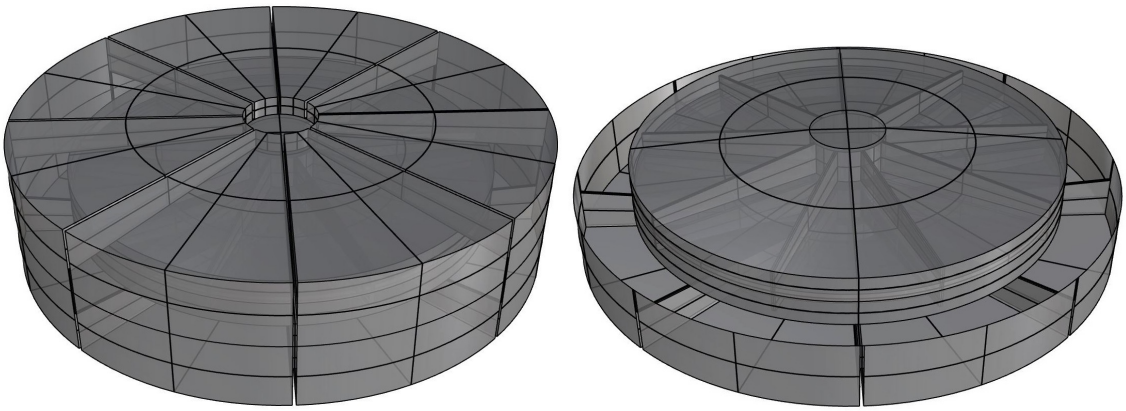

Figure 4: Left: NURBS-based IGA model of the VT arresting gear, including rotor, stator, and outer casing. Right: NURBS-based IGA model of the VT arresting gear with a zoom on the sliding interface between rotor and stator domains.

The VT arresting gear design includes two main parts: A rotating turbine (rotor) and a stationary reel (stator). The rotor diameter is 43.5 in. Looking at half of the rotor and stator, there are nine blades on the rotor side and eight vanes on the stator side, with a small gap present between the rotor blades and stator vanes. The rotor cross-section geometry is shown in Figure 2, while the key rotor geometric parameters and dimensions are summarized in Table 1.

Using this data input, the arresting gear fluid-mechanics-domain geometry is created with the help of the interactive geometry modeling and parametric design platform described in [45]. The generative algorithm employed for the rotor design is depicted in Figure 3. The algorithm, which is implemented using the visual programming interface Grasshopper, takes the rotor parametric input and, using the existing Rhino 3D functionality, constructs the underlying NURBS model of the arresting gear geometry. The resulting rotor geometric model is shown in Figure 2. The stator geometry is constructed in an analogous fashion. Figure 4 shows the complete arresting gear geometry, as well as a view of the model interior showing the sliding interface design. The sliding interface [48, 49] is needed for the fluid mechanics part of the FSI problem to account for the

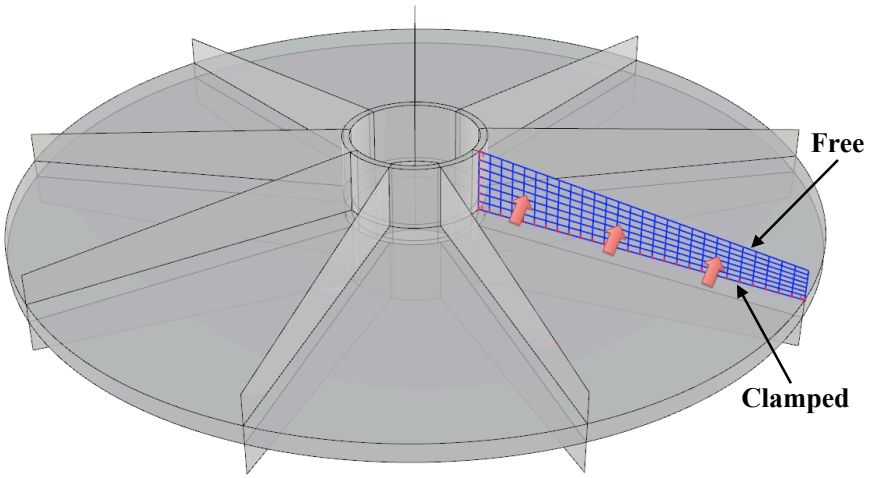

Figure 5: Rotor blade with clamped boundary conditions.

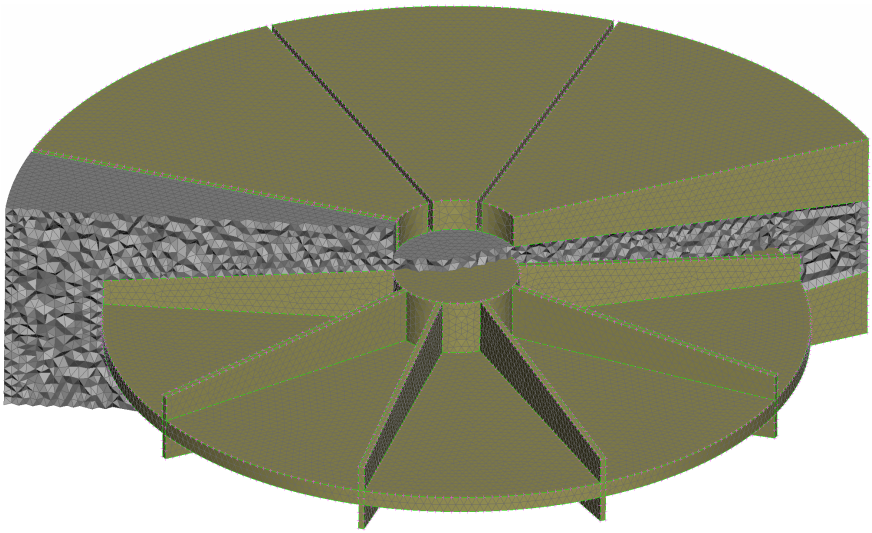

Figure 6: Tetrahedral mesh of the arresting-gear fluid-mechanics domain.

relative motion between the rotor and stator components. It is interesting to note that such objects as sliding interfaces may also be modeled within the proposed design platform, which is an added benefit of the approach employed.

In the FSI simulations, presented later in this article, the rotor blades are assumed to be flexible shell structures. The blade structural components are also created inside the parametric design platform. Figure 5 shows one of the blades superposed on the rotor model. Although the parametric design platform was created to build analysis-suitable models for IGA, here we take advantage of the modeling tool's direct compatibility with automatic FEM mesh generation software, and create the arresting-gear fluid-mechanics-domain mesh that consists of linear tetrahedral elements. The finest mesh makes use of about 2 million tetrahedra, and is shown in Figure 6.

3. Governing Equations and Numerical Methods

The hydrodynamics of the arresting gear is governed by the Navier–Stokes equations of incompressible flows, which are posed on a moving spatial domain and written in the Arbitrary Lagrangian–Eulerian (ALE) frame [50] as follows:

$$\rho_1 \left(\left. \frac{\partial \mathbf{u}}{\partial t} \right|_{\hat{x}} + (\mathbf{u} - \hat{\mathbf{u}}) \cdot \boldsymbol{\nabla} \mathbf{u} - \mathbf{f}_1 \right) - \boldsymbol{\nabla} \cdot \boldsymbol{\sigma}_1 = \mathbf{0}, \tag{1}$$

$$\boldsymbol{\nabla} \cdot \mathbf{u} = 0. \tag{2}$$

Here ρ_1 is the fluid density, $\mathbf{u}$ is the velocity, $\mathbf{f}_1$ is the body force per unit mass, and $\hat{\mathbf{u}}$ is the velocity of the fluid mechanics domain. The Cauchy stress, $\boldsymbol{\sigma}_1$, is given by

$$\boldsymbol{\sigma}_1 (\mathbf{u}, p) = -p\mathbf{I} + 2\mu\boldsymbol{\varepsilon}(\mathbf{u}), \tag{3}$$

where p is the pressure, $\mathbf{I}$ is the identity tensor, μ is the dynamic viscosity, and $\boldsymbol{\varepsilon}(\mathbf{u})$ is the strain-rate tensor defined as

$$\boldsymbol{\varepsilon}(\mathbf{u}) = \frac{\boldsymbol{\nabla} \mathbf{u} + \boldsymbol{\nabla} \mathbf{u}^T}{2}. \tag{4}$$

The time derivative in Eq. (1) is taken with respect to the fixed referential-domain coordinates $\hat{\mathbf{x}}$. All space derivatives are taken with respect to spatial coordinates of the current configuration $\mathbf{x}$.

The governing equations of structural mechanics are written in the Lagrangian frame [51] and consist of the local balance of linear momentum:

$$\rho_2 \left(\frac{\mathrm{d}^2 \mathbf{y}}{\mathrm{d}t^2} - \mathbf{f}_2 \right) - \boldsymbol{\nabla} \cdot \boldsymbol{\sigma}_2 = \mathbf{0}. \tag{5}$$

Here ρ_2 is the structural mass density, $\mathbf{f}_2$ is the body force per unit mass, $\boldsymbol{\sigma}_2$ is the Cauchy stress, and $\mathbf{y}$ is the unknown structural displacement. The time derivative in Eq. (5) is taken with respect to the fixed material coordinates of the structure reference configuration.

Compatibility of the kinematics and tractions is enforced at the fluid–structure interface, namely,

$$\mathbf{u} - \frac{\mathrm{d}\mathbf{y}}{\mathrm{d}t} = \mathbf{0}, \tag{6}$$

$$\boldsymbol{\sigma}_1 \mathbf{n}_1 + \boldsymbol{\sigma}_2 \mathbf{n}_2 = \mathbf{0}, \tag{7}$$

where $\mathbf{n}_1$ and $\mathbf{n}_2$ are the unit outward normal vectors to the fluid and structural mechanics domains, respectively.

To discretize the arresting-gear hydrodynamics, the ALE–VMS method [52, 53] and weakly enforced essential boundary conditions [54–56] are employed. The former is an extension of the residual-based variational multiscale (RBVMS) large eddy simulation (LES) turbulence model [57] to moving domains using the ALE technique, while the latter acts as a "near-wall model" in that it relaxes boundary-layer resolution requirements to achieve good accuracy of fluid solution and loads prediction on meshes without excessive boundary-layer refinement [58–63].

In the arresting gear design the stator is located in close proximity of the rotor, leaving only a small gap as the rotor blades pass the stator vanes during the device operation. To capture the complex dynamics of arresting-gear rotor-stator interaction, the sliding-interface technique from [48, 49] is employed. We note that a similar method, called the slip-interface technique, was proposed more recently in the context of space–time FEM in [64], as an alternative to other space-time methods [65–70] developed to address this class of computational challenges.

The structural mechanics of rotor blades (the stator vanes are assumed to be rigid) is modeled using Kirchhoff–Love shells [71, 72]. These are discretized using IGA based on NURBS [38, 39] and make use of only displacement degrees of freedom. Using rotation-free IGA shells to model the blades presents a good combination of efficiency, since no rotational degrees-of-freedom are employed, accuracy, since NURBS are a higher-order accurate discretization technique [73], and robustness.

The coupled FSI problem is formulated using an augmented Lagrangian approach for FSI, which was originally proposed in [35] to handle boundary-fitted mesh computations with non-matching fluid–structure interface discretizations. The key feature of the method is formal elimination of the Lagrange multiplier variable, which results in weak enforcement of the fluid–structure interface compatibility conditions using only primal variables (i.e., fluid velocity and pressure, and structure displacement), and, as a consequence, leads to increased efficiency compared to classical Lagrange-multiplier-based methods.

To accommodate the global rotor motion with superposed local blade elastic deformation, and to maintain a moving-mesh discretization, the fluid domain mesh is updated as follows. While at the fluid–structure interface the fluid mechanics mesh follows the motion of the blades, the outer boundaries of the rotor subdomain are restricted to only undergo rigid rotation. This choice of domain motion preserves the geometry of the sliding interface. The rest of the mesh motion is obtained by solving the equations of elastostatics with Jacobian-based stiffening [4, 74–78].

The generalized-α method [79–81] is employed to advance to FSI equations in time, while block-iterative coupling strategy [2–4, 32] is used to solve the coupled FSI system at each time step.

For a comprehensive discussion of numerical discretization techniques, coupling strategies, and application to a large class of problems in engineering we refer the reader to a recent book on

Table 2: Element and time-step sizes employed in the mesh convergence study.

	Mesh 1	Mesh 2	Mesh 3	Mesh 4
Element size (in)	3.0	2.0	1.0	0.5
Time step size (s)	7.5×10^{-4}	5.0×10^{-4}	2.5×10^{-4}	1.25×10^{-4}
Number of elements	16,395	49,644	314,462	2,008,047

Table 3: Rotor-torque values obtained in the mesh convergence study.

	Torque (ft lb)				
	Mesh 1	Mesh 2	Mesh 3	Mesh 4	Exp.
200 rpm	4,690	6,294	6,215	6,116	6,196
400 rpm	17,734	23,714	26,559	24,730	24,782
600 rpm	37,726	50,963	59,948	56,924	55,760
800 rpm	63,991	87,302	107,043	104,733	99,128

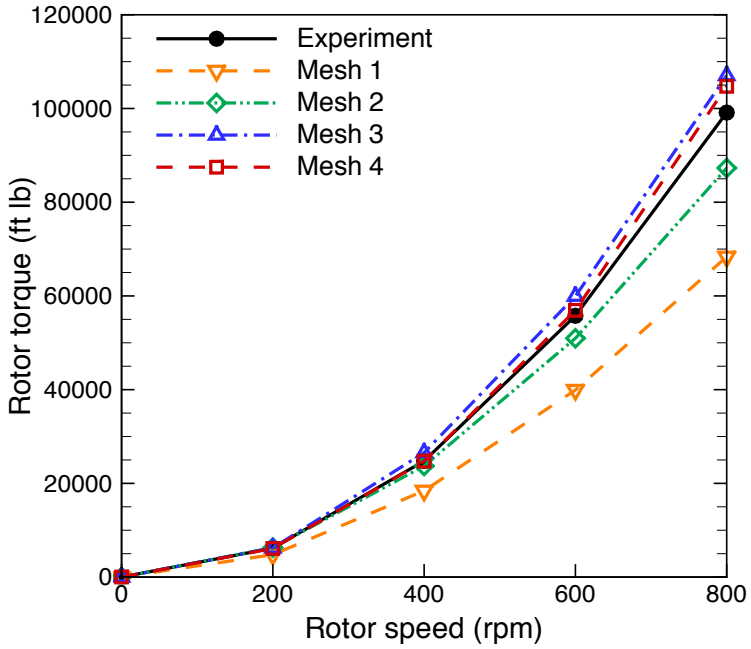

Figure 7: Rotor-torque values obtained in the mesh refinement study of the hydraulic arresting gear. Excellent mesh convergence results are achieved for all rotor speeds. Note that the mesh corresponding to the blue curve gives reasonably accurate results while consisting of only slightly over 300,000 elements.

computational FSI [32].

4. Simulations of the VT Arresting Gear Model

4.1. Mesh convergence study for the fluid mechanics simulation

We first perform standalone fluid mechanics computations assuming the structure is rigid and rotor speed is prescribed. Four cases corresponding to rotor speeds ranging from 200 rpm to

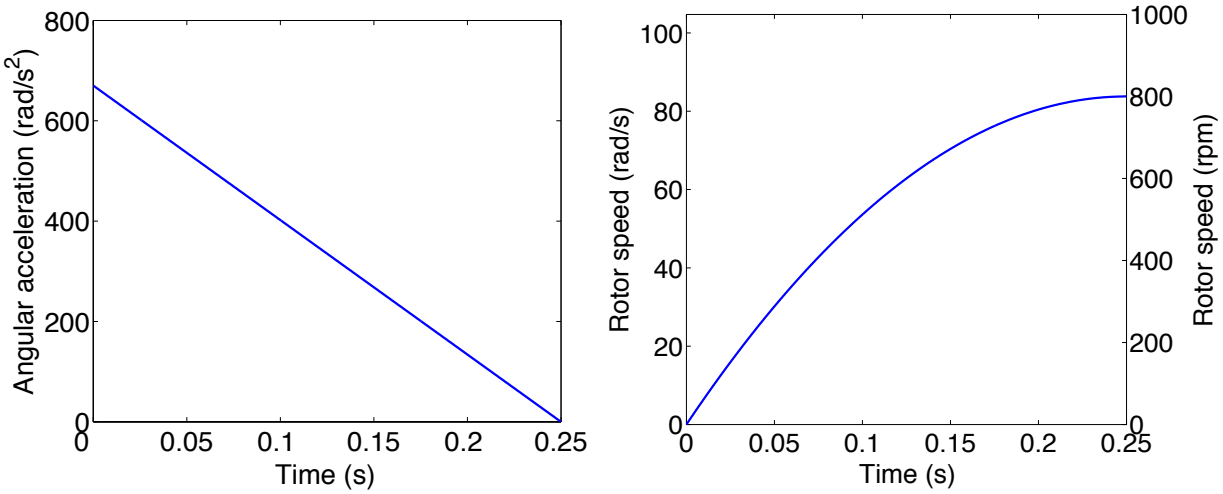

Figure 8: Left: Angular acceleration time history; Right: Rotor speed time history.

800 rpm at 200 rpm intervals are computed. Furthermore, mesh refinement in each case is performed to assess the mesh resolution requirements in achieving the desired level of accuracy in the rotor hydrodynamic torque prediction. Table 2 shows the element and time-step sizes employed in the mesh convergence study. For this study the simulations are started impulsively and continued until a statistically-stationary value of the rotor torque is achieved.

The results of the mesh refinement study are shown in Table 3 and Figure 7. Four meshes, with the numbers of elements given in Table 2, are employed for each rotor speed simulated. In all cases, good convergence of the numerical solution under mesh refinement is obtained. The converged results are in very good agreement with the experimental torque data. Note that, a coarse mesh of a little over 300,000 elements is already capable of producing accurate rotor loads, especially for lower-rpm cases.

Remark 1. We also note that such an excellent comparison between the simulation results and experimental data across a wide range of rotor speeds is achieved for this arresting gear model for the first time. The numerical results presented in [43], for example, obtained with a commercial code, showed a gross underestimation of the rotor torque without providing a good explanation for the discrepancies observed. In our opinion these were likely due to several factors, the most prominent being the lack of mesh resolution in combination with inadequate treatment of no-slip wall boundary conditions.

4.2. Ramp-up simulation

In this section we present a standalone fluid mechanics arresting-gear ramp-up simulation, which is representative of the device operation during the aircraft arrest. For this, we employ the second finest mesh in Table 2, and prescribe time-dependent rotor speed. We assume the rotor

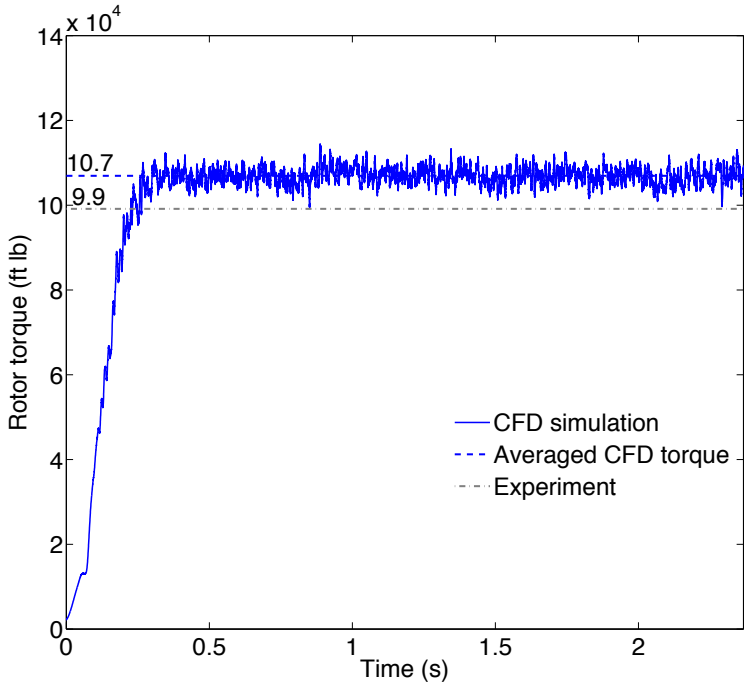

Figure 9: Time history of the rotor hydrodynamic torque for the terminal rotor speed of 800 rpm. Experimentally measured torque value at constant rotor speed of 800 rpm is plotted for comparison.

angular acceleration decreases from 670.2 rad/s^2 to zero within 0.25 s, at which point the rotor reaches the terminal speed of 800 rpm. Time history of the rotor acceleration and speed are plotted in Figure 8. The resulting rotor torque time history is shown in Figure 9. Within 0.25 s, the torque rapidly climbs to a statistically-stationary value that is consistent with the impulsive-start simulation results presented in Table 3 and Figure 7.

Figure 10 shows the flow speed isosurfaces at four different time instants as the rotor spins inside the arresting gear. The flow quickly transitions to turbulence and appears to be fully developed and statistically stationary soon after the terminal rotor speed is achieved. The full turbulent cascade, from large vortices to small eddies, is present inside the arresting gear, which is causing additional resistance to rotor motion. Instantaneous pressure contours on the rotor are shown in Figure 11. Note that the pressure distribution is not symmetric, which is in part due to the unsteady, turbulent nature of the flow, and in part due to the asymmetry of the arresting gear geometry stemming from the different number of rotor blades and stator vanes employed. Additionally, although the flow is unsteady and pressure fluctuates significantly, maximum pressure loads act somewhere between the blade midspan and tip. Also note that the magnitude of the suction pressure is as high as that of the positive stagnation pressure, and, in some cases, even exceeds it. These are important considerations in case one is trying to create a low fidelity fluid mechanics model as a surrogate for the high fidelity one.

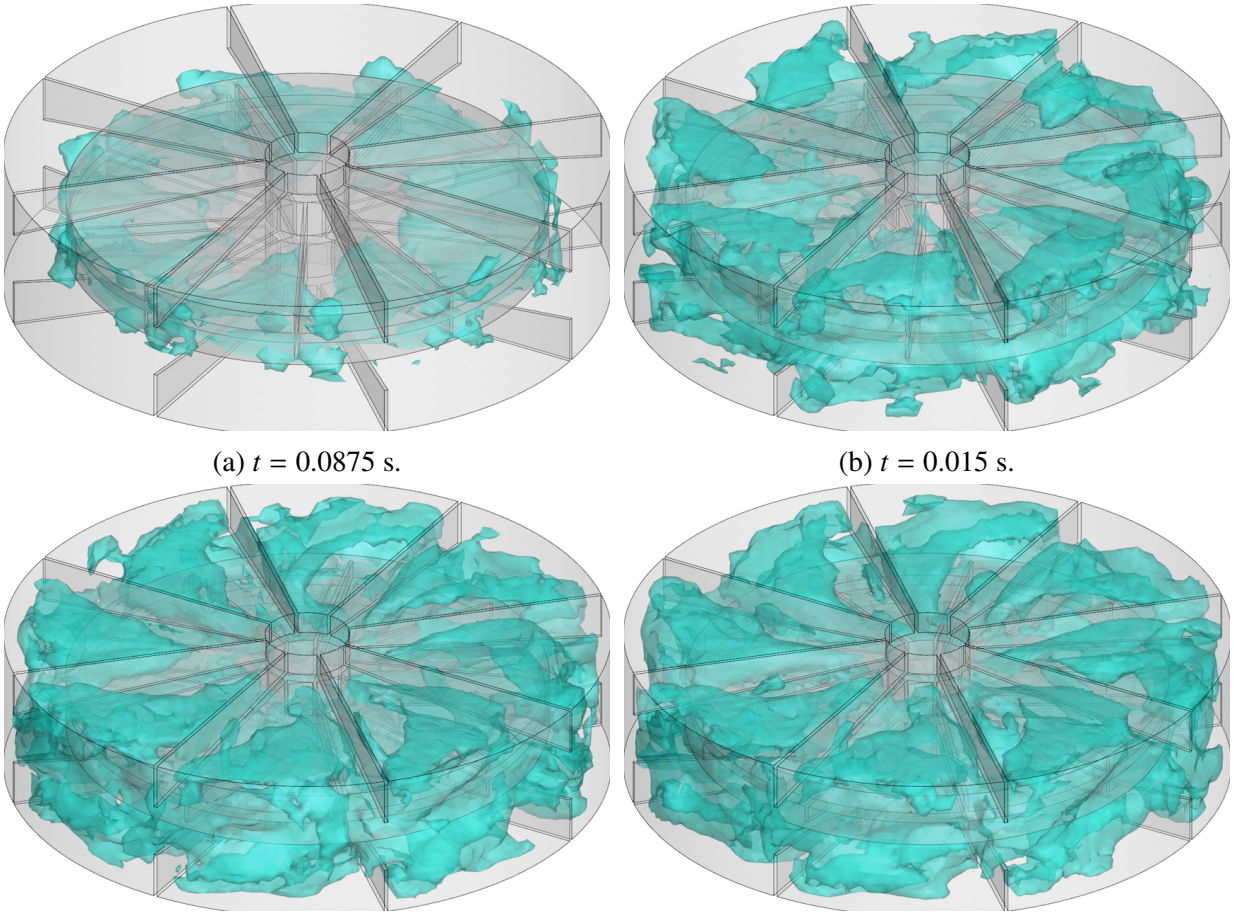

(a) t = 0.0875 s. (b) t = 0.015 s.

(c) t = 0.25 s. (d) t = 0.45 s.

Figure 10: Isosurfaces of water speed for the ramp-up simulation at different time instants showing the development of complex, recirculating turbulent flow.

4.3. Mesh convergence study for the structural mechanics simulation

In this section we perform a mesh convergence study for the arresting gear blade structure. We first compute the blade structural response under prescribed static constant pressure load. The applied pressure of 139 psi is chosen to match the total rotor torque of 99,128 ft lb, which is the experimentally reported value for the rotor speed of 800 rpm. We also perform the rotor blade natural frequency computations. The blade is assumed to be clamped to the rotor hub and disc, which results in the boundary conditions shown in Figure 5. The blade material properties correspond to that of stainless steel, which is isotropic and has Young's modulus of 29,007.5 ksi, Poisson's ratio of 0.27, and mass density of 499.4 lb/ft^3. The blade is also assumed to have a constant thickness of 0.348 in.

Both maximum displacement under the pressure load and blade fundamental frequency exhibit good convergence with mesh refinement as shown in Figure 12. The third mesh, which is comprised of cubic NURBS and has about 300 control points, produces essentially converged values

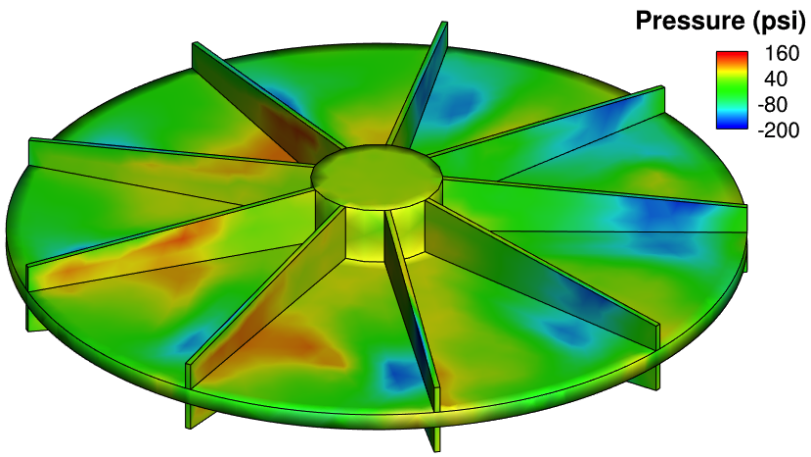

Figure 11: Pressure (in psi) on the rotor surface at a time instant after the terminal rotor speed is reached. Note that the pressure solution is completely non symmetric, which is a consequence of the unsteady, turbulent nature of the flow, and the asymmetry of the arresting gear geometry stemming from the different number of rotor blades and stator vanes employed.

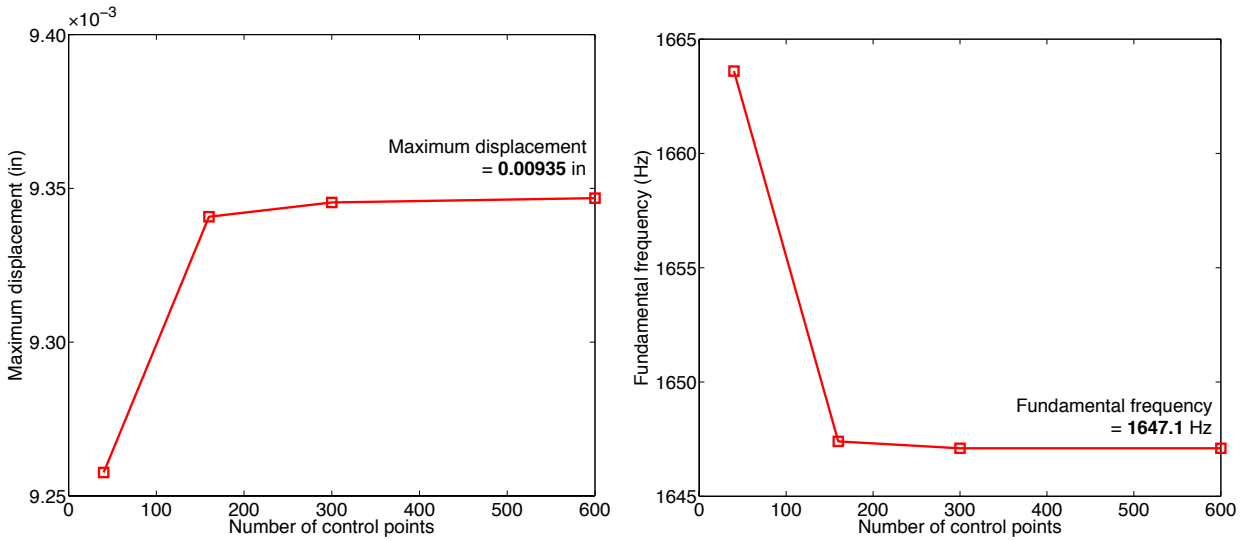

(a) Maximum displacement.

(b) Fundamental frequency.

Figure 12: Mesh convergence study for a single-blade structural mechanics simulation.

for both quantities, and is thus chosen for the FSI simulations presented in the sequel. Figure 13 shows contours of the blade displacement magnitude and maximum in-plane principal Green–Lagrange strain (MIPE) for the pressure load case. Maximum displacement reaches 0.00935 in at the top free edge. The highest MIPE is concentrated around the bottom clamped edge, and is located directly below the region of maximum blade deflection.

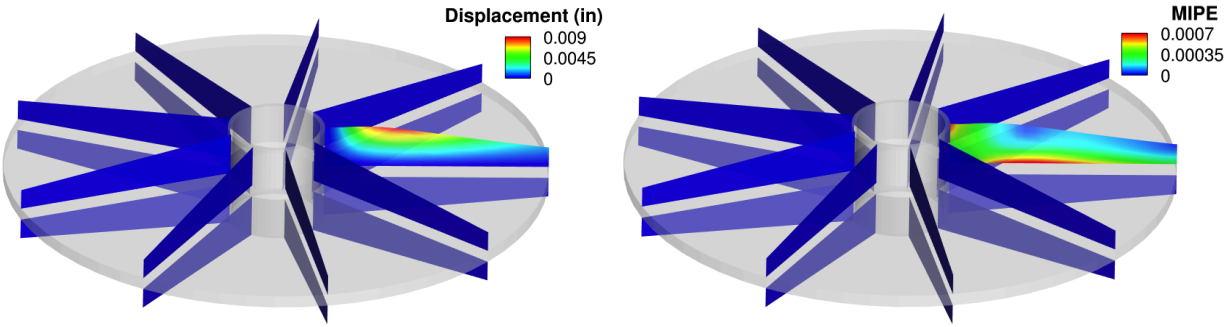

(a) Displacement magnitude. (b) MIPE.

Figure 13: Single-blade structural mechanics simulation.

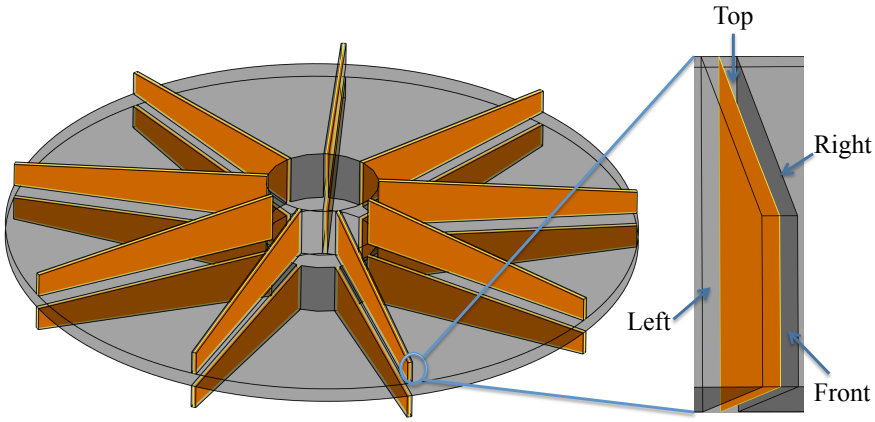

Figure 14: Fluid mechanics domain built with an assumption of a solid blade superposed with the blade structural shell midsurface. This discretization choice creates a geometric and parametric mismatch between the fluid and structural meshes at their interface. However, such situations are naturally handled in the FSI framework employed in this study.

4.4. FSI simulation

In this section we present FSI simulation results for the VT arresting gear model. In the model the casing, the middle plate, and the stator vanes are assumed to be rigid, while the rotor blades are assumed to be flexible. Because the fluid mechanics mesh is built with an assumption of a solid blade, while a shell model is used for the blade structure, the fluid and structural meshes are mismatched both geometrically and parametrically at their interface (see Figure 14). However, the FSI framework employed here is naturally suited for such situations [35].

We perform FSI simulations using ramp-up conditions described in Section 4.2, which lead to the terminal rotor speed of 800 rpm. We test two cases corresponding to the blade thickness of 0.348 in (Case 1) and 0.226 in (Case 2). Figure 15 shows instantaneous blade-structure deformed configuration and the surrounding turbulent flow field for Case 1.

We extract the displacement histories for two spatial locations, labeled No. 271 and No. 288, and shown in Figure 16. The displacement magnitude at both locations is shown, in the time and frequency domains, in Figures 17 and 18. Although the thinner Case 2 exhibits displacement

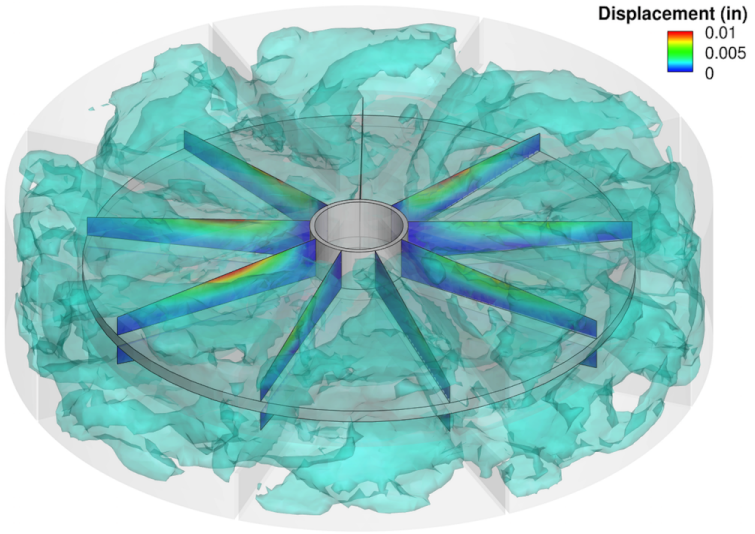

Figure 15: Rotor blade deflection contours superposed with the flow speed isosurfaces for Case 1.

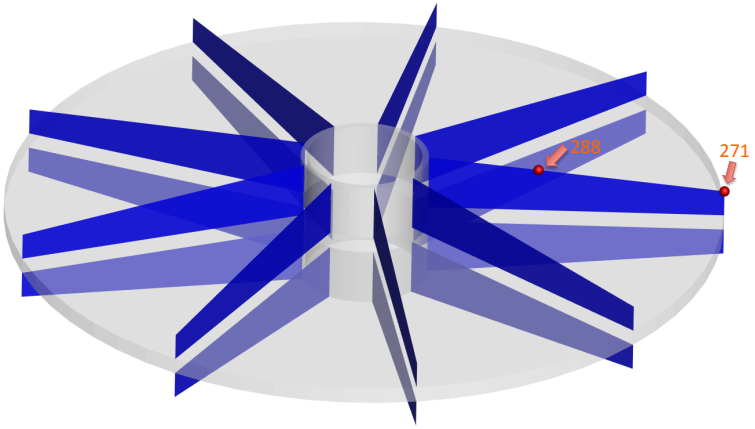

Figure 16: Two spatial locations on the blade midsurface where the displacement time history is analyzed.

levels that are 2.5 times larger than Case 1, the blade displacement magnitudes are relatively small compared to the device length scale in both cases. The frequency of rotor-stator interaction (i.e., the frequency at which the rotor blade passes the stator vane) is 106.67 Hz. That frequency is clearly visible in the frequency-domain displacement plots. Several harmonics of that frequency are also excited in the blade response, which is especially pronounced for the thinner blade at location No. 288. Contours of the blade displacement and MIPE are shown in Figures 19 and 20.

The rotor-torque time history, including comparison between the FSI and rigid-rotor simulations, is shown in Figure 21. Due to the relatively small blade deformation, the mean values of the torque are similar for the FSI and rigid-rotor simulations. As expected, the thinner blade gives a more pronounced FSI effect. The frequency content, however, is quite different for the FSI and rigid-rotor simulations, especially for Case 2. In the FSI computation much higher frequencies are produced in the rotor-torque signal than in the rigid-rotor computation.

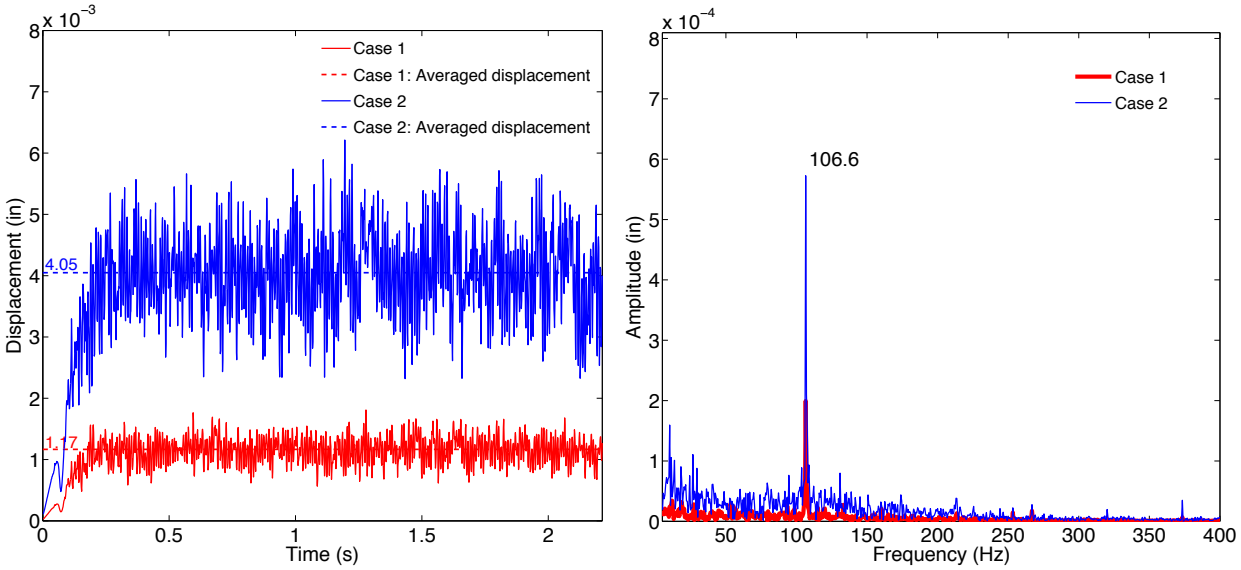

(a) Time domain plot. (b) Frequency domain plot.

Figure 17: Blade displacement magnitude at location No. 271.

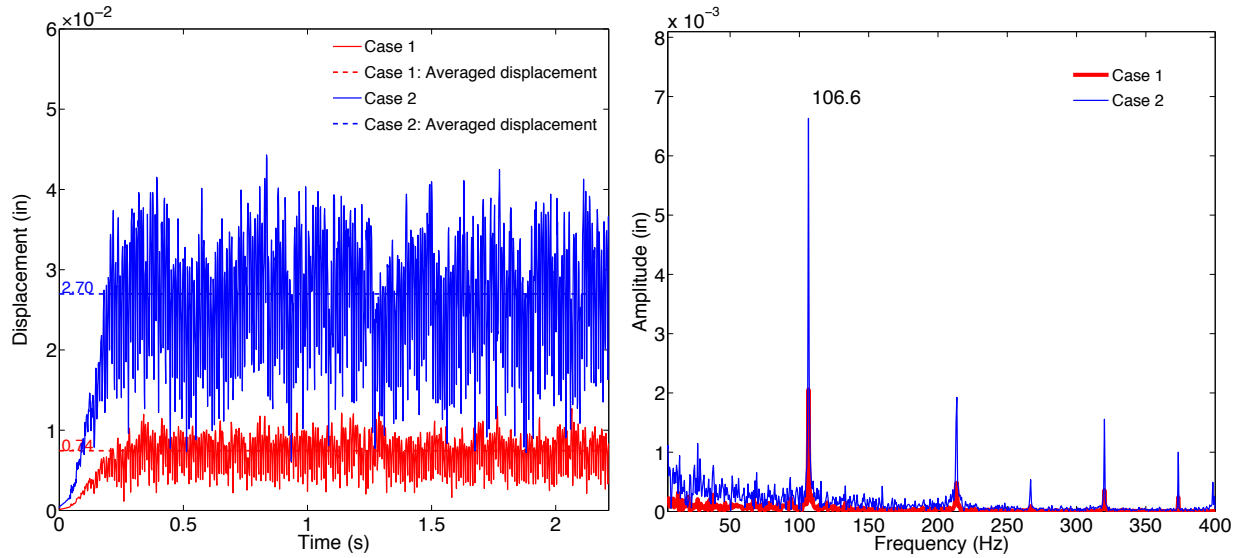

(a) Time domain plot. (b) Frequency domain plot.

Figure 18: Blade displacement magnitude at location No. 288.

Remark 2. The computations reported in this work are carried out in a parallel computing environment on a cluster with compute nodes consisting of two eight-core Xeon E5-2680 2.7GHz processors and 32GB of memory. A description of the parallelization strategy employed may be found in [82]. Using Mesh 3 as an example, for both standalone fluid mechanics and FSI simulations, the fluid mesh is partitioned into 18 subdomains using METIS [83], and each subdomain is assigned to a processor core. The structural mesh for a single blade is not partitioned. However,

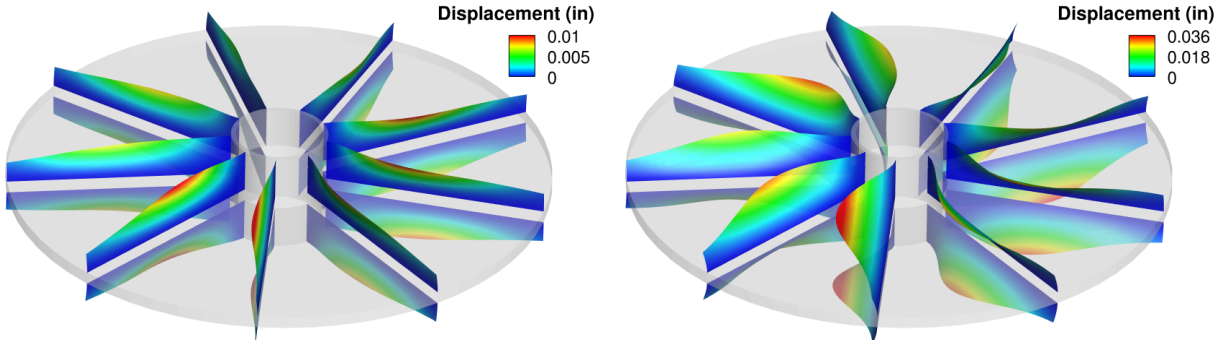

(a) Case 1. (b) Case 2.

Figure 19: Contours of blade displacement magnitude. (A scaling factor of 100 is applied to the displacement for visualization.)

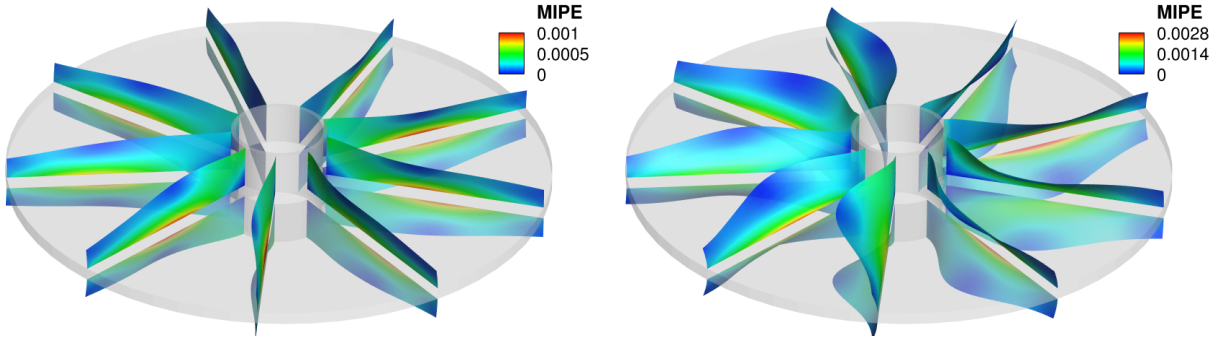

(a) Case 1. (b) Case 2.

Figure 20: Contours of MIPE. (A scaling factor of 100 is applied to the displacement for visualization.)

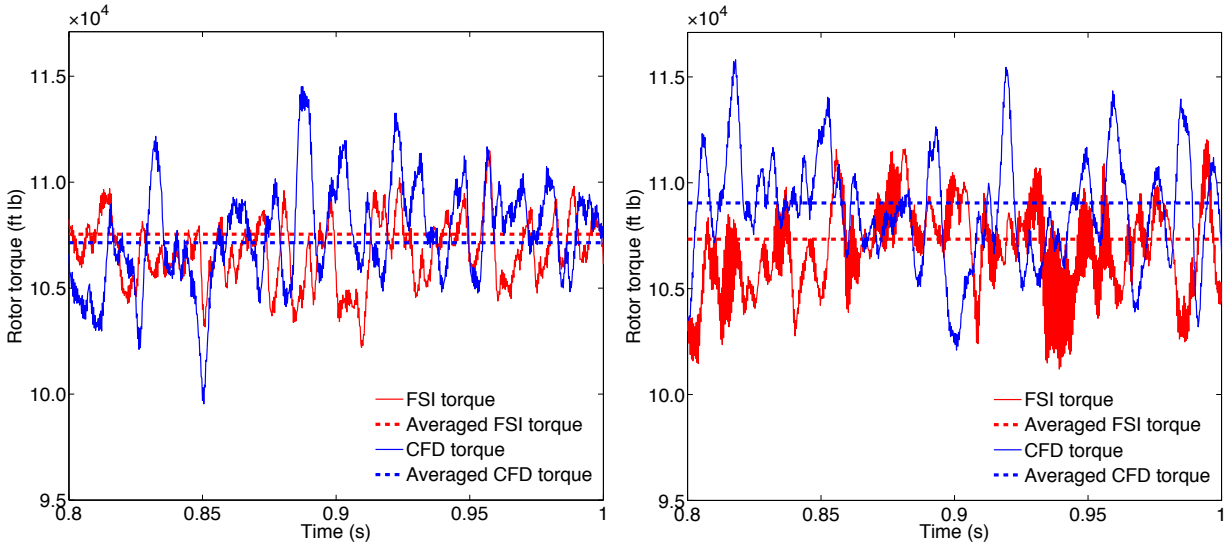

(a) Case 1. (b) Case 2.

Figure 21: Rotor-torque time history for FSI and rigid-rotor simulations, the latter denoted by "CFD torque".

each blade is assigned to a different processor core to improve overall efficiency. For the simulations in Figure 21b, we use three Newton iterations per time step, with 100 to 125 diagonally-preconditioned-GMRES iterations. The standalone fluid mechanics and FSI computations take 1.8 and 2.7 hours, respectively, to run 500 time steps.

5. Conclusion

In this work we developed a "pipeline" for geometry modeling and predictive FSI simulation of hydraulic arresting gears at full scale. A parametric modeling platform recently proposed in [45] was adapted to generate analysis-suitable IGA models for this complex system. The FSI simulations were carried out for the VT arresting gear model using a combination of IGA to discretize the structural mechanics part, and FEM to discretize the hydrodynamics part of the coupled problem. Careful mesh convergence studies were performed for standalone fluid and structural analyses of the VT arresting gear model. One of the findings of the mesh convergence study was that despite the underlying complexity of the turbulent flow inside the arresting gear, a relatively modest size of fluid mechanics mesh was needed to accurately capture the rotor hydrodynamic loads. This good accuracy is attributable to the use of the ALE-VMS technique with weakly enforced boundary conditions as the underlying numerical methodology. The FSI simulations produced rotor blade displacements that are relatively low compared to the device length scale. However, the vibrational response predicted the presence of multiple highly pronounced frequencies, especially for the thinner blade design. This finding is intriguing and needs to be investigated in the future work.

Acknowledgements

This work was supported by NAVAIR, Program Manager Dr. Nam Phan, and ARO grant No. W911NF-14-1-0296, Program Manager Dr. Joseph Myers. This support is gratefully acknowledged.

References

[1] T. E. Tezduyar, S. Sathe, R. Keedy, and K. Stein. Space–time techniques for finite element computation of flows with moving boundaries and interfaces. In S. Gallegos, I. Herrera, S. Botello, F. Zarate, and G. Ayala, editors, *Proceedings of the III International Congress on Numerical Methods in Engineering and Applied Science*. CD-ROM, Monterrey, Mexico, 2004.

[2] T. E. Tezduyar, S. Sathe, R. Keedy, and K. Stein. Space–time finite element techniques for computation of fluid–structure interactions. *Computer Methods in Applied Mechanics and Engineering*, 195:2002–2027, 2006.

[3] T. E. Tezduyar, S. Sathe, and K. Stein. Solution techniques for the fully-discretized equations in computation of fluid–structure interactions with the space–time formulations. *Computer Methods in Applied Mechanics and Engineering*, 195:5743–5753, 2006.

[4] T. E. Tezduyar and S. Sathe. Modeling of fluid–structure interactions with the space–time finite elements: Solution techniques. *International Journal for Numerical Methods in Fluids*, 54:855–900, 2007.

[5] K. Takizawa, S. Wright, C. Moorman, and T. E. Tezduyar. Fluid–structure interaction modeling of parachute clusters. *International Journal for Numerical Methods in Fluids*, 65:286–307, 2011.

[6] K. Takizawa, T. Spielman, and T. E. Tezduyar. Space–time FSI modeling and dynamical analysis of spacecraft parachutes and parachute clusters. *Computational Mechanics*, 48:345–364, 2011.

[7] K. Takizawa and T. E. Tezduyar. Computational methods for parachute fluid–structure interactions. *Archives of Computational Methods in Engineering*, 19:125–169, 2012.

[8] K. Takizawa, T. E. Tezduyar, J. Boben, N. Kostov, C. Boswell, and A. Buscher. Fluid–structure interaction modeling of clusters of spacecraft parachutes with modified geometric porosity. *Computational Mechanics*, 52:1351–1364, 2013.

[9] K. Takizawa, D. Montes, M. Fritze, S. McIntyre, J. Boben, and T. E. Tezduyar. Methods for FSI modeling of spacecraft parachute dynamics and cover separation. *Mathematical Models and Methods in Applied Sciences*, 23:307–338, 2013.

[10] K. Takizawa, T. E. Tezduyar, C. Boswell, R. Kolesar, and K. Montel. FSI modeling of the reefed stages and disreefing of the Orion spacecraft parachutes. *Computational Mechanics*, 54:1203–1220, 2014.

[11] K. Takizawa, T. E. Tezduyar, R. Kolesar, C. Boswell, T. Kanai, and K. Montel. Multiscale methods for gore curvature calculations from FSI modeling of spacecraft parachutes. *Computational Mechanics*, 54:1461–1476, 2014.

[12] K. Takizawa, T. E. Tezduyar, C. Boswell, Y. Tsutsui, and K. Montel. Special methods for aerodynamic-moment calculations from parachute FSI modeling. *Computational Mechanics*, 55:1059–1069, 2015.

[13] K. Takizawa, T. E. Tezduyar, and R. Kolesar. FSI modeling of the Orion spacecraft drogue parachutes. *Computational Mechanics*, 55:1167–1179, 2015.

[14] Y. Bazilevs, M.-C. Hsu, D. Benson, S. Sankaran, and A. Marsden. Computational fluid–structure interaction: Methods and application to a total cavopulmonary connection. *Computational Mechanics*, 45:77–89, 2009.

[15] Y. Bazilevs, M.-C. Hsu, Y. Zhang, W. Wang, X. Liang, T. Kvamsdal, R. Brekken, and J. Isaksen. A fully-coupled fluid–structure interaction simulation of cerebral aneurysms. *Computational Mechanics*, 46:3–16, 2010.

[16] Y. Bazilevs, M.-C. Hsu, Y. Zhang, W. Wang, T. Kvamsdal, S. Hentschel, and J. Isaksen. Computational fluid–structure interaction: Methods and application to cerebral aneurysms. *Biomechanics and Modeling in Mechanobiology*, 9:481–498, 2010.

[17] M.-C. Hsu and Y. Bazilevs. Blood vessel tissue prestress modeling for vascular fluid–structure interaction simulations. *Finite Elements in Analysis and Design*, 47:593–599, 2011.

[18] C. C. Long, M.-C. Hsu, Y. Bazilevs, J. A. Feinstein, and A. L. Marsden. Fluid–structure interaction simulations of the Fontan procedure using variable wall properties. *International Journal for Numerical Methods in Biomedical Engineering*, 28:512–527, 2012.

[19] K. Takizawa, K. Schjodt, A. Puntel, N. Kostov, and T. E. Tezduyar. Patient-specific computational analysis of the influence of a stent on the unsteady flow in cerebral aneurysms. *Computational Mechanics*, 51:1061–1073, 2013.

[20] K. Takizawa, H. Takagi, T. E. Tezduyar, and R. Torii. Estimation of element-based zero-stress state for arterial FSI computations. *Computational Mechanics*, 54:895–910, 2014.

[21] K. Takizawa, T. E. Tezduyar, A. Buscher, and S. Asada. Space-time interface-tracking with topology change (ST-TC). *Computational Mechanics*, 54:955–971, 2014.

[22] K. Takizawa. Computational engineering analysis with the new-generation space–time methods. *Computational Mechanics*, 54:193–211, 2014.

[23] K. Takizawa, Y. Bazilevs, T. E. Tezduyar, C. C. Long, A. L. Marsden, and K. Schjodt. ST and ALE-VMS methods for patient-specific cardiovascular fluid mechanics modeling. *Mathematical Models and Methods in Applied Sciences*, 24:2437–2486, 2014.

[24] K. Takizawa, T. E. Tezduyar, A Buscher, and S. Asada. Space–time fluid mechanics computation of heart valve models. *Computational Mechanics*, 54:973–986, 2014.

[25] K. Takizawa, R. Torii, H. Takagi, T. E. Tezduyar, and X. Y. Xu. Coronary arterial dynamics computation with medical-image-based time-dependent anatomical models and element-based zero-stress state estimates. *Computational Mechanics*, 54:1047–1053, 2014.

[26] C. C. Long, A. L. Marsden, and Y. Bazilevs. Fluid–structure interaction simulation of pulsatile ventricular assist devices. *Computational Mechanics*, 52:971–981, 2013.

[27] C. C. Long, M. Esmaily-Moghadam, A. L. Marsden, and Y. Bazilevs. Computation of residence time in the simulation of pulsatile ventricular assist devices. *Computational Mechanics*, 54:911–919, 2014.

[28] C. C. Long, A. L. Marsden, and Y. Bazilevs. Shape optimization of pulsatile ventricular assist devices using FSI to minimize thrombotic risk. *Computational Mechanics*, 54:921–932, 2014.

[29] M.-C. Hsu, D. Kamensky, Y. Bazilevs, M. S. Sacks, and T. J. R. Hughes. Fluid–structure interaction analysis of bioprosthetic heart valves: significance of arterial wall deformation. *Computational Mechanics*, 54:1055–1071, 2014.

[30] M.-C. Hsu, D. Kamensky, F. Xu, J. Kiendl, C. Wang, M. C. H. Wu, J. Mineroff, A. Reali, Y. Bazilevs, and M. S. Sacks. Dynamic and fluid–structure interaction simulations of bioprosthetic heart valves using parametric design with T-splines and Fung-type material models. *Computational Mechanics*, 55:1211–1225, 2015.

[31] D. Kamensky, M.-C. Hsu, D. Schillinger, J. A. Evans, A. Aggarwal, Y. Bazilevs, M. S. Sacks, and T. J. R. Hughes. An immersogeometric variational framework for fluid-structure interaction: Application to bioprosthetic heart valves. *Computer Methods in Applied Mechanics and Engineering*, 284:1005–1053, 2015.

[32] Y. Bazilevs, K. Takizawa, and T. E. Tezduyar. *Computational Fluid–Structure Interaction: Methods and Applications*. Wiley, 2013.

[33] Y. Bazilevs, K. Takizawa, and T. E. Tezduyar. Challenges and directions in computational fluid–structure interaction. *Mathematical Models and Methods in Applied Sciences*, 23:215–221, 2013.

[34] K. Takizawa, D. Montes, S. McIntyre, and T. E. Tezduyar. Space–time VMS methods for modeling of incompressible flows at high Reynolds numbers. *Mathematical Models and Methods in Applied Sciences*, 23:223–248, 2013.

[35] Y. Bazilevs, M.-C. Hsu, and M. A. Scott. Isogeometric fluid–structure interaction analysis with emphasis on non-matching discretizations, and with application to wind turbines. *Computer Methods in Applied Mechanics and Engineering*, 249-252:28–41, 2012.

[36] K. Takizawa and T. E. Tezduyar. Space–time computation techniques with continuous representation in time (ST-C). *Computational Mechanics*, 53:91–99, 2014.

[37] K. Takizawa, T. E. Tezduyar, and T. Kuraishi. Multiscale ST methods for thermo-fluid analysis of a ground vehicle and its tires. *Mathematical Models and Methods in Applied Sciences*, 25:2227–2255, 2015.

[38] T. J. R. Hughes, J. A. Cottrell, and Y. Bazilevs. Isogeometric analysis: CAD, finite elements, NURBS, exact geometry, and mesh refinement. *Computer Methods in Applied Mechanics and Engineering*, 194:4135–4195, 2005.

[39] J. A. Cottrell, T. J. R. Hughes, and Y. Bazilevs. *Isogeometric Analysis: Toward Integration of CAD and FEA*. Wiley, Chichester, 2009.

[40] L. Piegl and W. Tiller. *The NURBS Book (Monographs in Visual Communication), 2nd ed.* Springer-Verlag, New York, 1997.

[41] Autodesk T-Splines Plug-in for Rhino. http://www.tsplines.com/products/tsplines-for-rhino.html. 2015.

[42] M. A. Scott, T. J. R. Hughes, T. W. Sederberg, and M. T. Sederberg. An integrated approach to engineering design and analysis using the Autodesk T-spline plugin for Rhino3d. ICES REPORT 14-33, The Institute for Computational Engineering and Sciences, The University of Texas at Austin, September 2014, 2014.

[43] Y.-T. Chiu. Computational fluid dynamics simulations of hydraulic energy absorber. Master's thesis, Virginia Polytechnic Institute and State University, 1999.

[44] R. V. Parker. Arrestment considerations for the space shuttle. In *The Space Congress Proceedings*, Wilmington, Delaware, 1971.

[45] M.-C. Hsu, C. Wang, A. G. Herrema, D. Schillinger, A. Ghoshal, and Y. Bazilevs. An interactive geometry modeling and parametric design platform for isogeometric analysis. *Computers & Mathematics with Applications*, 2015. http://dx.doi.org/10.1016/j.camwa.2015.04.002.

[46] Rhinoceros. http://www.rhino3d.com/. 2015.

[47] Grasshopper. http://www.grasshopper3d.com/. 2015.

[48] Y. Bazilevs and T. J. R. Hughes. NURBS-based isogeometric analysis for the computation of flows about rotating components. *Computational Mechanics*, 43:143–150, 2008.

[49] M.-C. Hsu and Y. Bazilevs. Fluid–structure interaction modeling of wind turbines: simulating the full machine. *Computational Mechanics*, 50:821–833, 2012.

[50] T. J. R. Hughes, W. K. Liu, and T. K. Zimmermann. Lagrangian–Eulerian finite element formulation for incompressible viscous flows. *Computer Methods in Applied Mechanics and Engineering*, 29:329–349, 1981.

[51] T. Belytschko, W. K. Liu, and B. Moran. *Nonlinear Finite Elements for Continua and Structures*. Wiley, 2000.

[52] K. Takizawa, Y. Bazilevs, and T. E. Tezduyar. Space–time and ALE-VMS techniques for patient-specific cardiovascular fluid–structure interaction modeling. *Archives of Computational Methods in Engineering*, 19:171–225, 2012.

[53] Y. Bazilevs, M.-C. Hsu, K. Takizawa, and T. E. Tezduyar. ALE-VMS and ST-VMS methods for computer modeling of wind-turbine rotor aerodynamics and fluid–structure interaction. *Mathematical Models and Methods in Applied Sciences*, 22(supp02):1230002, 2012.

[54] Y. Bazilevs and T. J. R. Hughes. Weak imposition of Dirichlet boundary conditions in fluid mechanics. *Computers and Fluids*, 36:12–26, 2007.

[55] Y. Bazilevs, C. Michler, V. M. Calo, and T. J. R. Hughes. Weak Dirichlet boundary conditions for wall-bounded turbulent flows. *Computer Methods in Applied Mechanics and Engineering*, 196:4853–4862, 2007.

[56] Y. Bazilevs, C. Michler, V. M. Calo, and T. J. R. Hughes. Isogeometric variational multiscale modeling of wall-bounded turbulent flows with weakly enforced boundary conditions on unstretched meshes. *Computer Methods in Applied Mechanics and Engineering*, 199:780–790, 2010.

[57] Y. Bazilevs, V. M. Calo, J. A. Cottrel, T. J. R. Hughes, A. Reali, and G. Scovazzi. Variational multiscale residual-based turbulence modeling for large eddy simulation of incompressible flows. *Computer Methods in Applied Mechanics and Engineering*, 197:173–201, 2007.

[58] I. Akkerman, Y. Bazilevs, C. E. Kees, and M. W. Farthing. Isogeometric analysis of free-surface flow. *Journal of Computational Physics*, 230:4137–4152, 2011.

[59] C. E. Kees, I. Akkerman, M. W. Farthing, and Y. Bazilevs. A conservative level set method suitable for variable-order approximations and unstructured meshes. *Journal of Computational Physics*, 230:4536–4558, 2011.

[60] I. Akkerman, Y. Bazilevs, D. J. Benson, M. W. Farthing, and C. E. Kees. Free-surface flow and fluid–object interaction modeling with emphasis on ship hydrodynamics. *Journal of Applied Mechanics*, 79:010905, 2012.

[61] M.-C. Hsu, I. Akkerman, and Y. Bazilevs. Wind turbine aerodynamics using ALE–VMS: Validation and the role of weakly enforced boundary conditions. *Computational Mechanics*, 50:499–511, 2012. doi:10.1007/s00466-012-0686-x.

[62] I. Akkerman, J. Dunaway, J. Kvandal, J. Spinks, and Y. Bazilevs. Toward free-surface modeling of planing vessels: simulation of the Fridsma hull using ALE-VMS. *Computational Mechanics*, 50:719–727, 2012.

[63] M.-C. Hsu, I. Akkerman, and Y. Bazilevs. Finite element simulation of wind turbine aerodynamics: Validation study using NREL Phase VI experiment. *Wind Energy*, 17:461–481, 2014.

[64] K. Takizawa, T. E. Tezduyar, H. Mochizuki, H. Hattori, S. Mei, L. Pan, and K. Montel. Space–time VMS method for flow computations with slip interfaces (ST-SI). *Mathematical Models and Methods in Applied Sciences*, 25:2377–2406, 2015.

[65] K. Takizawa, T. E. Tezduyar, S. McIntyre, N. Kostov, R. Kolesar, and C. Habluetzel. Space–time VMS computation of wind-turbine rotor and tower aerodynamics. *Computational Mechanics*, 53:1–15, 2014.

[66] K. Takizawa, T. E. Tezduyar, and N. Kostov. Sequentially-coupled space–time FSI analysis of bio-inspired flapping-wing aerodynamics of an MAV. *Computational Mechanics*, 54:213–233, 2014.

[67] K. Takizawa, Y. Bazilevs, T. E. Tezduyar, M.-C. Hsu, O. Øiseth, K. M. Mathisen, N. Kostov, and S. McIntyre. Engineering analysis and design with ALE-VMS and space–time methods. *Archives of Computational Methods in Engineering*, 21:481–508, 2014.

[68] Y. Bazilevs, K. Takizawa, T. E. Tezduyar, M.-C. Hsu, N. Kostov, and S. McIntyre. Aerodynamic and FSI analysis of wind turbines with the ALE–VMS and ST–VMS methods. *Archives of Computational Methods in Engineering*, 21:359–398, 2014.

[69] K. Takizawa, T. E. Tezduyar, and A. Buscher. Space–time computational analysis of MAV flapping-wing aerodynamics with wing clapping. *Computational Mechanics*, 55:1131–1141, 2015.

[70] Y. Bazilevs, K. Takizawa, and T. E. Tezduyar. New directions and challenging computations in fluid dynamics modeling with stabilized and multiscale methods. *Mathematical Models and Methods in Applied Sciences*, 25:2217–2226, 2015.

[71] J. Kiendl, K.-U. Bletzinger, J. Linhard, and R. Wüchner. Isogeometric shell analysis with Kirchhoff–Love elements. *Computer Methods in Applied Mechanics and Engineering*, 198:3902–3914, 2009.

[72] J. Kiendl, Y. Bazilevs, M.-C. Hsu, R. Wüchner, and K.-U. Bletzinger. The bending strip method for isogeometric analysis of Kirchhoff–Love shell structures comprised of multiple patches. *Computer Methods in Applied Mechanics and Engineering*, 199:2403–2416, 2010.

[73] Y. Bazilevs, L. Beirao da Veiga, J. A. Cottrell, T. J. R. Hughes, and G. Sangalli. Isogeometric analysis: Approximation, stability and error estimates for *h*-refined meshes. *Mathematical Models and Methods in Applied Sciences*, 16:1031–1090, 2006.

[74] T. E. Tezduyar, M. Behr, S. Mittal, and A. A. Johnson. Computation of unsteady incompressible flows with the finite element methods – space–time formulations, iterative strategies and massively parallel implementations. In *New Methods in Transient Analysis*, PVP-Vol.246/AMD-Vol.143, pages 7–24, New York, 1992. ASME.

[75] T. Tezduyar, S. Aliabadi, M. Behr, A. Johnson, and S. Mittal. Parallel finite-element computation of 3D flows. *Computer*, 26(10):27–36, 1993.

[76] A. A. Johnson and T. E. Tezduyar. Mesh update strategies in parallel finite element computations of flow problems with moving boundaries and interfaces. *Computer Methods in Applied Mechanics and Engineering*, 119:73–94, 1994.

[77] T. E. Tezduyar. Finite element methods for flow problems with moving boundaries and interfaces. *Archives of Computational Methods in Engineering*, 8:83–130, 2001.

[78] K. Stein, T. Tezduyar, and R. Benney. Mesh moving techniques for fluid–structure interactions with large displacements. *Journal of Applied Mechanics*, 70:58–63, 2003.

[79] Y. Bazilevs, V. M. Calo, T. J. R. Hughes, and Y. Zhang. Isogeometric fluid–structure interaction: theory, algorithms, and computations. *Computational Mechanics*, 43:3–37, 2008.

[80] J. Chung and G. M. Hulbert. A time integration algorithm for structural dynamics withimproved numerical dissipation: The generalized-α method. *Journal of Applied Mechanics*, 60:371–75, 1993.

[81] K. E. Jansen, C. H. Whiting, and G. M. Hulbert. A generalized-α method for integrating the filtered Navier-Stokes equations with a stabilized finite element method. *Computer Methods in Applied Mechanics and Engineering*, 190:305–319, 2000.

[82] M.-C. Hsu, I. Akkerman, and Y. Bazilevs. High-performance computing of wind turbine aerodynamics using isogeometric analysis. *Computers & Fluids*, 49:93–100, 2011.

[83] G. Karypis and V. Kumar. A fast and high quality multilevel scheme for partitioning irregular graphs. *SIAM Journal on Scientific Computing*, 20:359–392, 1999.